The Presence of the Temporal Horn Exacerbates the Vulnerability of Hippocampus During Head Impacts

Zhou Zhou[1,2*†], Xiaogai Li[2†], August G. Domel[1], Emily L. Dennis[3,4], Marios Georgiadis[4], Yuzhe Liu[1], Samuel J. Raymond[1], Gerald Grant[5,6], Svein Kleiven[2†], David Camarillo[1,5,7‡] and Michael Zeineh[4*‡]

[1]Department of Bioengineering, Stanford University, Stanford, CA, United States, [2]Neuronic Engineering, KTH Royal Institute of Technology, Stockholm, Sweden, [3]TBI and Concussion Center, Department of Neurology, University of Utah, Salt Lake City, UT, United States, [4]Department of Radiology, Stanford University, Stanford, CA, United States, [5]Department of Neurosurgery, Stanford University, Stanford, CA, United States, [6]Department of Neurology, Stanford University, Stanford, CA, United States, [7]Department of Mechanical Engineering, Stanford University, Stanford, CA, United States

Hippocampal injury is common in traumatic brain injury (TBI) patients, but the underlying pathogenesis remains elusive. In this study, we hypothesize that the presence of the adjacent fluid-containing temporal horn exacerbates the biomechanical vulnerability of the hippocampus. Two finite element models of the human head were used to investigate this hypothesis, one with and one without the temporal horn, and both including a detailed hippocampal subfield delineation. A fluid-structure interaction coupling approach was used to simulate the brain-ventricle interface, in which the intraventricular cerebrospinal fluid was represented by an arbitrary Lagrangian-Eulerian multi-material formation to account for its fluid behavior. By comparing the response of these two models under identical loadings, the model that included the temporal horn predicted increased magnitudes of strain and strain rate in the hippocampus with respect to its counterpart without the temporal horn. This specifically affected cornu ammonis (CA) 1 (CA1), CA2/3, hippocampal tail, subiculum, and the adjacent amygdala and ventral diencephalon. These computational results suggest that the presence of the temporal horn exacerbate the vulnerability of the hippocampus, highlighting the mechanobiological dependency of the hippocampus on the temporal horn.

Keywords: hippocampal injury, temporal horn, brain-ventricle interface, fluid-structure interaction, finite element analysis, traumatic brain injury

INTRODUCTION

Traumatic brain injury (TBI) is a critical public health and socio-economic problem. In the United States, approximately 5.3 million people are living with a TBI-related disability (Langlois and Sattin, 2005). At a global level, an estimated 69 million people suffer a TBI each year (Dewan et al., 2018), with yearly costs reaching 400 billion dollars (Maas et al., 2017). Despite worldwide efforts to reduce the incidence and mitigate the consequence of TBI, improvement of overall outcome has not been achieved (Roozenbeek et al., 2013), especially for mild TBI (mTBI), also known as concussion. Epidemiological data showed that concussion rates in high school sports (Rosenthal et al., 2014) and the military (Cameron et al., 2012) have been rising. The need to improve concussion outcome is particularly urgent, given that concussion is notoriously underreported, difficult to

screen, and associated with immediate and persistent deficit to memory and attention with possible chronic neurodegenerative consequences (McKee et al., 2015; Meier et al., 2015).

As a crucial structure for long-term, episodic memory formation and retrieval (Bird and Burgess, 2008), the hippocampus is often reported to be injured secondary to physical trauma in humans across different impact severities. In fatal TBI, post-mortem histopathological examinations identify the hippocampus as one of the most commonly injured regions (73%–87%) (Kotapka et al., 1992; Kotapka et al., 1993; Kotapka et al., 1994; Maxwell et al., 2003). In mTBI, *in vivo* human imaging analyses demonstrate that repetitive concussive impacts or even sub-concussive impacts (i.e., high-velocity impacts that do not cause concussion) are associated with abnormal hippocampal atrophy longitudinally (Parivash et al., 2019) and cross-sectionally (Singh et al., 2014). The prevalence of hippocampal injury has also been widely noted in animal experiments (e.g., non-human primates, pigs, rats, sheep, and rabbits) under diverse modes of mechanical perturbations, including non-impact acceleration (Gennarelli et al., 1982; Kotapka et al., 1991), impact acceleration (Anderson et al., 2003), weight-drops (Kalish and Whalen, 2016), cortical contusion (Baldwin et al., 1997), and fluid percussion injury (Hicks et al., 1996). The resultant injury within the hippocampus of experimentally traumatized animals exhibits a broad spectrum of pathological manifestations, varying from impaired electrophysiological activity associated with hippocampal circuitry dysfunction (Wolf et al., 2017) to profound neuronal apoptosis and marked gliosis (Smith et al., 1997).

The pathogenetic mechanism of trauma-induced hippocampal injury has long been attributed to the selective vulnerability of hippocampal neurons to hypoxemia and ischemia (Pulsinelli, 1985; Ng et al., 1989), typical complications of severe TBI insults (Graham et al., 1978; Graham et al., 1989). For example, a histopathological study revealed that 27 out of 29 individuals with at least one episode of clinically recorded hypoxia had hippocampal damage (Kotapka et al., 1992). However, 14 out of 18 patients without documented hypoxemia also had hippocampal lesions (Kotapka et al., 1992), suggesting that hippocampal injury may be independent of hypoxia. Another candidate mechanism is pathological neuronal excitation involving glutamate and/or other excitatory amino acid neurotransmitters, supported by animal experiments where traumatic insults triggered glutamate concentrations in the extracellular fluid of the hippocampus (Faden et al., 1989; Runnerstam et al., 2001). Given that the hippocampus is dense in receptors for glutamate (Kotapka et al., 1991; Leranth et al., 1996), redundant extracellular glutamate could induce neuronal excitotoxicity, and indeed, pre-treatment of experimentally traumatized animals with glutamate antagonists attenuates hippocampal lesions (Faden et al., 1989). However, such antagonists in humans have not proven beneficial, thus, a neuroexcitotoxic mechanism in human TBI cannot be considered a sole explanation (Parsons et al., 1999). Taken together, trauma-induced hippocampal lesions in humans cannot be fully explained by the current mechanisms.
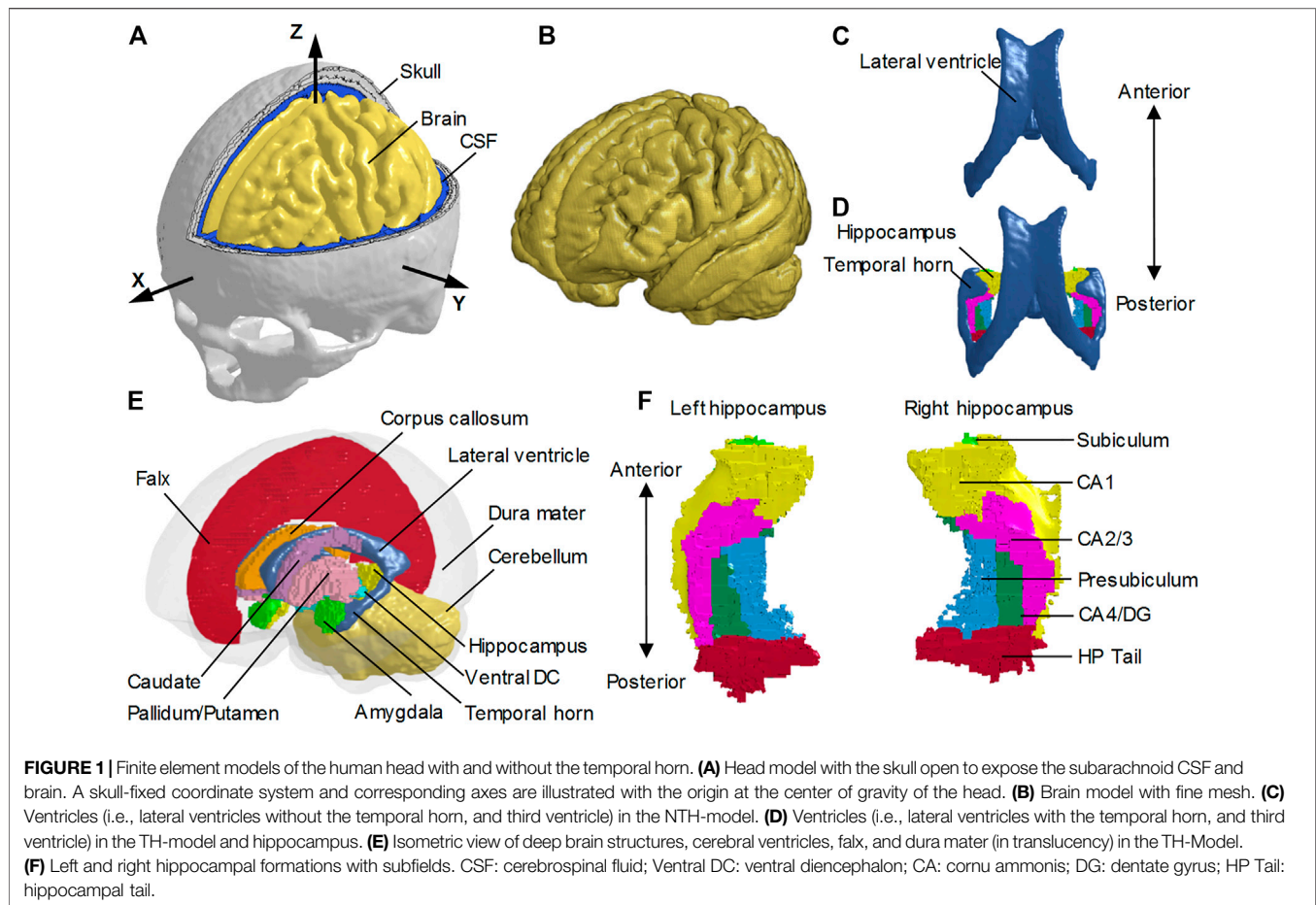
An alternative line of investigation is biomechanical. Given that previous modeling work has shown that the presence of fluid can affect the transmission of mechanical forces within the brain (Zhou et al., 2020a), one structure that may be associated with the hippocampal vulnerability is the temporal horn of the lateral ventricle. The temporal horn is a cavity that forms the roof of the hippocampus and is filled with cerebrospinal fluid (CSF) and occasionally choroid plexus (Insausti and Amaral, 2003). Previous studies found that the volumes of the hippocampus and temporal horn were inversely correlated in TBI patients (Gale et al., 1994; Bigler et al., 1997; Bigler et al., 2002). However, the biomechanical effect of the temporal horn on the hippocampus remains unknown.

Interrogation of this biomechanical relationship requires modeling to estimate the myriad variables and forces at play. As computational surrogates of the human head, finite element (FE) models have been instrumental in exploring the association of regional vulnerabilities with potential predisposing factors during trauma from the biomechanical perspective (Kleiven, 2007; McAllister et al., 2012; Mao et al., 2013; Ji et al., 2015; Atsumi et al., 2018; Trotta et al., 2020; Zhou et al., 2021a). Extending the current models to investigate the relationship between the temporal horn and hippocampus requires that the FE model possesses an anatomically and mechanically accurate representation of both structures, and a precise description of the interface between the fluid-filled temporal horn and neighboring hippocampus. However, in existing finite element models, the temporal horn was either wholly substituted as brain parenchyma (McAllister et al., 2012; Zhou et al., 2016) or simulated as a solid structure using the Lagrangian approach (Kleiven, 2007; Mao et al., 2013; Ji et al., 2015; Atsumi et al., 2018; Trotta et al., 2020; Zhou et al., 2021a). This Lagrangian approach is a dominant numerical scheme for solid mechanics and is insufficient to computationally reflect the fact that the temporal horn is filled with CSF with the potential flow within the ventricular cavity during the impacts (Souli et al., 2000; Zhou, 2019; Zhou et al., 2020b). Approaches to date may have missed key and relevant properties of the temporal horn that have precluded the determination of its biomechanical relevance.

The aim of the current study was to discern whether the presence of the temporal horn exacerbates the biomechanical vulnerability of the hippocampus. To test this hypothesis, two models with and without a detailed anatomic description of the temporal horn profiles are established. By comparing the strain-related responses to identical loadings between the two models, the biomechanical mechanism for the temporal horn's role in the vulnerability of the hippocampus was uncovered.

MATERIALS AND METHODS

In this study, we employed computational modeling to discern the biomechanical dependency of the hippocampus on the temporal horn. To achieve that, we utilized a novel, multi-million element 3D head model (Zhou et al., 2020a) that did not initially incorporate the temporal horn (no-temporal-horn (NTH)-model), and further extended this model by adding the

FIGURE 1 | Finite element models of the human head with and without the temporal horn. **(A)** Head model with the skull open to expose the subarachnoid CSF and brain. A skull-fixed coordinate system and corresponding axes are illustrated with the origin at the center of gravity of the head. **(B)** Brain model with fine mesh. **(C)** Ventricles (i.e., lateral ventricles without the temporal horn, and third ventricle) in the NTH-model. **(D)** Ventricles (i.e., lateral ventricles with the temporal horn, and third ventricle) in the TH-model and hippocampus. **(E)** Isometric view of deep brain structures, cerebral ventricles, falx, and dura mater (in translucency) in the TH-Model. **(F)** Left and right hippocampal formations with subfields. CSF: cerebrospinal fluid; Ventral DC: ventral diencephalon; CA: cornu ammonis; DG: dentate gyrus; HP Tail: hippocampal tail.
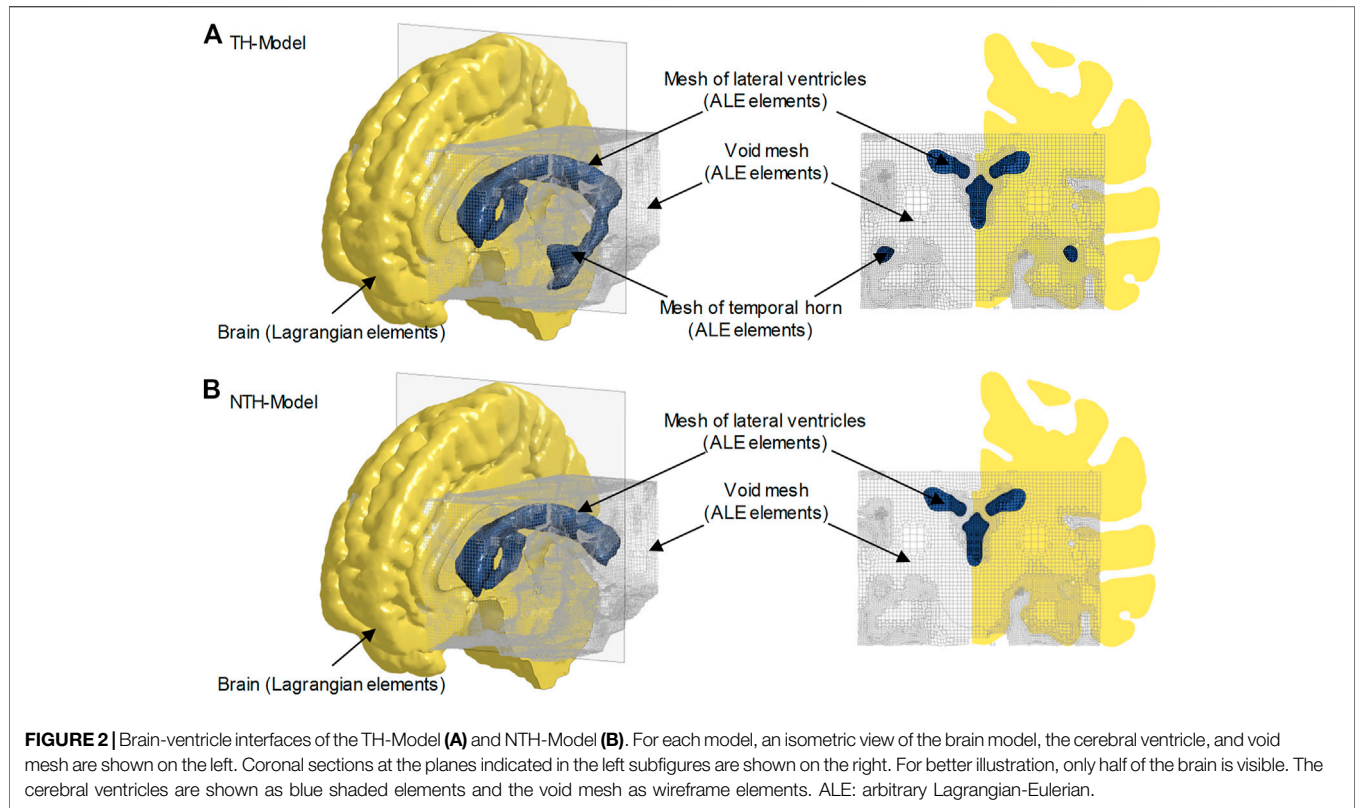
temporal horn to the lateral ventricle (temporal-horn (TH)-Model). An arbitrary Lagrangian-Eulerian (ALE) multi-material formation was used to emulate the fluid behavior of the intraventricular CSF, with its responses being concatenated with the brain tissue via a fluid-structure interaction (FSI) coupling algorithm. This allows computation of strain (fractional change in unit length), strain rate (strain change over time), and stress (force per unit area) in the hippocampus. By comparing the deformation-related responses estimated by these two models secondary to six concussive/sub-concussive impacts, the mechanical role that the temporal horn exerted on the hippocampus was revealed.

Finite Element Modeling of Human Brain

The FE head model without the temporal horn (i.e., the NTH-Model) used in this study was previously developed at KTH Royal Institute of Technology in Stockholm, Sweden (Zhou et al., 2020a). The model includes the scalp, skull, brain, subarachnoid CSF (i.e., CSF within the subarachnoid space), meninges (i.e., dura mater and pia mater), falx, tentorium, and cerebral ventricles (i.e., lateral ventricles without the temporal horn, and third ventricle) (**Figure 1**). The whole head model consists of 4.2 million hexahedral elements and 0.5 million quadrilateral elements, in which the brain has a total of 2.6 million nodes, and 2.3 million hexahedral elements. The

average brain element size is 0.59 ± 0.26 mm, meeting the requirement that a human brain model with converged responses should have an average element size less than 1.8 mm (Zhao and Ji, 2019). Information regarding the geometry profiles and material modeling of various intracranial components in the NTH-Model was elaborated in a previous study (Zhou et al., 2020a) as well as in **Supplementary Appendix SAA**.

To investigate the potential effect of the presence of the CSF-filled temporal horn on the hippocampus, we extended the NTH-model by adding the fluid-filled temporal horn to the cerebral ventricle (i.e., from **Figure 1C** to **Figure 1D**). This extended model (i.e., the TH-Model) has the same geometrical features, material properties, element formulation, and interface conditions as the NTH-Model, except for the newly added temporal horn. The volume ratio between the temporal horn and the brain in the TH-Model was 0.13%, falling within the range in healthy adults (0.1%–0.3%) (Bigler and Tate, 2001). Strain response and brain-skull relative motion estimated by the TH-Model were respectively evaluated by the experiments presented by Hardy et al. (2007) and Zhou et al. (2019c) in **Supplementary Appendix SAB**. Details about the cerebral ventricle modeling and the brain-ventricle interface of the TH-Model are elaborated in the following two sections, along with that in the NTH-Model.

FIGURE 2 | Brain-ventricle interfaces of the TH-Model **(A)** and NTH-Model **(B)**. For each model, an isometric view of the brain model, the cerebral ventricle, and void mesh are shown on the left. Coronal sections at the planes indicated in the left subfigures are shown on the right. For better illustration, only half of the brain is visible. The cerebral ventricles are shown as blue shaded elements and the void mesh as wireframe elements. ALE: arbitrary Lagrangian-Eulerian.

TABLE 1 | Material constant for the cerebral ventricles in the TH-Model and NTH-Model. P: pressure, C: intercept of $v_s - v_p$ curves, v_s: velocity of a shockwave traveling through the intermediary material, v_p: velocity of the shocked material; S1, S2, and S3: coefficients of the slope of the $v_s - v_p$ curves, γ_0: Gruneisen gamma, a: first order volume correction to γ_0; ρ_0: initial density; ρ: instantaneous density; σ_{ij}^v: deviatoric stress; γ: dynamic viscosity; $\dot{\varepsilon}_{ij}'$: deviatoric strain rate; PC: cut-off pressure.

Equation of state	ρ_0 (kg/m3)	C (m/s)	S_1	S_2	S_3	a	γ_0
$P = \frac{\rho_0 C^2 \mu (1+(1-\gamma^2/2)\mu - a/2\mu^2)}{[1-(S_1-1)\mu - S_2\mu^2/(\mu+1) - S_3\mu^3/(\mu+1)^2]}$; $\mu = \frac{\rho}{\rho_0} - 1$	1000	1482.9	2.10	-0.17	0.01	0	1.2
Constitutive equation	γ (Pa.s)	PC (MPa)					
$\sigma_{ij}^v = \gamma \dot{\varepsilon}_{ij}'$	0.001	−22					

To facilitate the derivation of deformation-related metrics in regions of interest (ROIs) from completed simulations, the brain segmentation was registered to the coordinate system of the FE head model and then the brain elements were grouped into different sub-regions according to the spatial correspondence with the brain segmentation *via* an automated procedure implemented by a custom-built MATLAB script. For both the TH-Model and NTH-Model, the anatomically classified brain regions included cerebral cortex, cerebellum, hippocampus with six subfields as segmented by FreeSurfer 7 (i.e., cornu ammonis (CA) 1, CA2/3, CA4/dentate gyrus (DG), hippocampus tail (HP Tail), subiculum, and presubiculum) (**Figure 1F**), and non-hippocampal paraventricular regions [i.e., amygdala, ventral diencephalon (ventral DC), pallidum, putamen, caudate, and corpus callosum (CC)] (**Figure 1E**).

Cerebral Ventricle Modeling

To emulate the fluid properties of the intraventricular CSF and potential CSF flow secondary to exterior loading, the cerebral ventricles in the TH-Model (**Figure 2A**) and NTH-Model (**Figure 2B**) were simulated using an ALE multi-material formulation. This formulation advances the solution in time using a two-step operation, in which the material is antecedently deformed in a Lagrangian step and subsequently followed by an advection step with the element variables being remapped (Zhou et al., 2019b). In the Lagrangian step, the intraventricular CSF deformation was determined by the equation of state (for dilatational responses) and constitutive equation (for deviatoric responses) listed in **Table 1**, together with associated formulations and material constants. In the advection step, a second-order van Leer scheme was selected, excelling in advection accuracy and numerical stability (Van Leer, 1979).

TABLE 2 | Peaks of translational acceleration and rotational acceleration and injury severity of the six cases considered in this study. The X, Y, and Z axes are the same as those in the skull-fixed coordinate system in **Figure 1A**. Note that Cases 1–2 and Cases 4–5 are on-field impacts measured by the mouthguard (Hernandez et al., 2015), while Case 3 and Case 6 are laboratory-reconstructed impacts (Pellman et al., 2003; Sanchez et al., 2019).

Case ID	Peak translational acceleration (g)				Peak rotational acceleration (krad/s^2)				Injury severity
	X	Y	Z	Magnitude	X	Y	Z	Magnitude	
Case 1	−40.6	100.4	−63.4	106.1	12.89	−3.06	−3.24	12.95	Concussion
Case 2	−61.1	−57.8	−45.8	84.2	4.21	5.14	−1.84	6.19	Concussion
Case 3	−31.9	133.4	41.6	134.0	4.65	1.20	−6.81	7.50	Concussion
Case 4	−49.3	−47.2	−32.3	71.9	2.44	−4.36	−7.26	7.75	Sub-concussion
Case 5	7.3	18.1	11.4	20.4	4.12	0.59	1.05	4.14	Sub-concussion
Case 6	−21.5	−59.4	57.8	78.8	−5.82	−1.66	−2.44	6.24	Sub-concussion

Brain-Ventricle Interface Modeling

To couple the mechanical responses of the ALE-represented intraventricular CSF with the Lagrangian-represented brain, a penalty-based FSI coupling scheme (Batterbee et al., 2011; Zhou et al., 2019a) was implemented to both the TH-Model and NTH-Model. The implemented coupling scheme delivers tension and compression in the radial direction and allows relative motion in the tangential direction.

Owing to the requirement of implementing the penalty-based coupling scheme, any locations to which the fluid may potentially flow during the simulations are required to be meshed. Considering that the intraventricular CSF might flow to regions that were originally occupied by deep brain structures (due to deformation of the brain itself and the relative motion between the brain and cerebral ventricles during the simulation), additional meshes were generated in these regions, referred to as the "void mesh" in **Figure 2A** and **Figure 2B**, and initially overlapped with part of the brain elements. The void mesh was emulated with the ALE multi-material element approach, with material properties identical to that of the intraventricular CSF (**Table 1**) along with an extra void definition. Such a void definition ensured that no fluid was distributed within the void mesh under its initial configuration. The motion of the ALE elements followed the mass-weighted velocity in the ALE mesh (Hallquist, 2007).

Loading Conditions

Estimation of hippocampal response was obtained from the TH-Model and NTH-Model by simulating six representative football head impacts (**Table 2** and **Supplementary Appendix SAB**). At Stanford University, instrumented mouthguards have been developed to measure six-degree-of-freedom head kinematics during in-game head impacts to athletes (Liu et al., 2020; Cecchi et al., 2021). Using these instrumented mouthguards, over 500 head impacts in football have been video confirmed (Hernandez et al., 2015). In the current study, two concussive impacts, one with the athlete suffering alteration of consciousness (Case 1) and the other with the player having a milder but self-reported concussion (Case 2), and two sub-concussive impacts (Case 4 and Case 5) were simulated. In addition, a helmet-to-helmet collision involving two players was simulated with the struck player (Case 3) having a concussion and the striking player not (Case 6). Video recordings of the game were analyzed, through which the initial head kinematics were determined and further guided the laboratory reconstruction to

obtain the dynamic kinematics of this collision (Pellman et al., 2003; Sanchez et al., 2019). All simulations were solved by the massively parallel processing version of LS-DYNA R11 double precision with 128 processors.

Data Analysis

For each computational simulation, the strains and strain rates in the six hippocampal subfields, the whole hippocampus, and six non-hippocampal periventricular regions were extracted from the TH-Model and NTH-Model, resulting in a total of 13 region-wise comparisons for each injury metric. This was motivated by the findings that hippocampal cell death was significantly affected by the strain (Cater et al., 2006) and hippocampal functional impairment was dependent on both strain and strain rate (Kang and Morrison, 2015) in *in vitro* TBI models on organotypic hippocampal slice cultures from rat. At each timestep, the element-wise strain and strain rate values were calculated as the first principal value of the Green-Lagrange strain tensor and the first principal value of rate of deformation tensor (Holzapfel, 2000). The element-wise strain and strain rate peaks were then identified as the maximum value of the strain and strain rate values across all timesteps. For each ROI, the element-wise strain and strain rate peaks of all affiliated elements were analyzed. To eliminate potential numerical artifacts (Panzer et al., 2012; Zhou et al., 2021b), the 95th percentile values of element-wise strain peaks and element-wise strain rate peaks were respectively regarded as the strain peak and strain rate peak of the given region. A total of 13 ROIs, including six hippocampal subfields, the whole hippocampus, and six non-hippocampal paraventricular regions were considered in the current study. To quantify the variation in the responses per the inclusion of temporal horn, percentage differences in region-wise strain and strain rate peaks were computed for all ROIs in each loading case, with the value from the NTH-Model as reference. Similar postprocessing procedures have been implemented in previous studies (Gabler et al., 2018; Hajiaghamemar et al., 2020; Wu et al., 2021) to extract the regional-wise strain/strain rate peaks.

In total, six impacts were simulated by the TH-Model and NTH-Model, respectively. To statistically ascertain the influence of temporal horn on the deformation-related responses across the six impacts, the strain and strain rate peaks of all six impacts estimated by the TH-Model and NTH-Model were analyzed with a Wilcoxon matched-pairs signed-rank test (N = 6), using an uncorrected significance threshold of $p < 0.05$. This test was respectively implemented to all the 13 ROIs. Due to the small
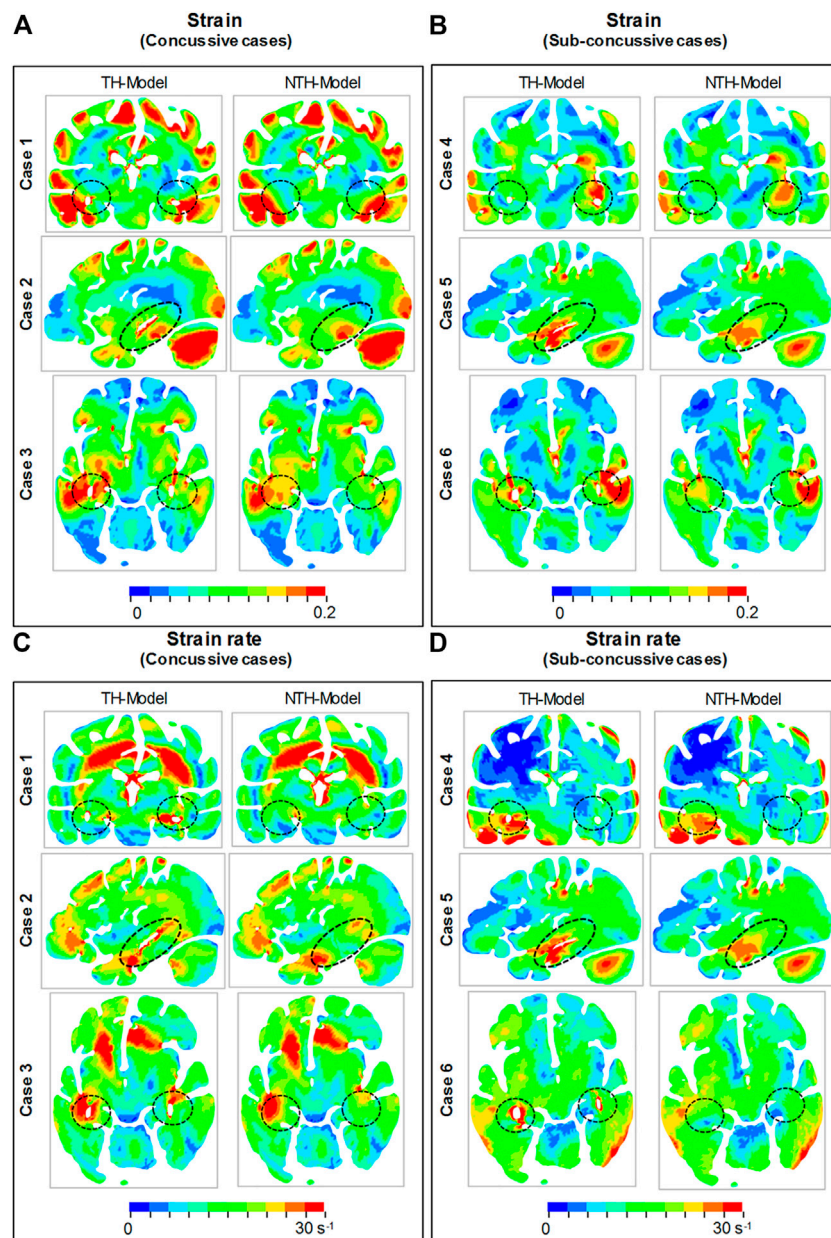
FIGURE 3 | Comparison of the maximum principal strain **(A,B)** and strain rate **(C,D)** distribution between the TH-model and NTH-model for three concussive and three sub-concussive impacts (Cases 1–3 and 4–6 respectively). The temporal horn and adjacent tissue are highlighted by black dashed ellipses.

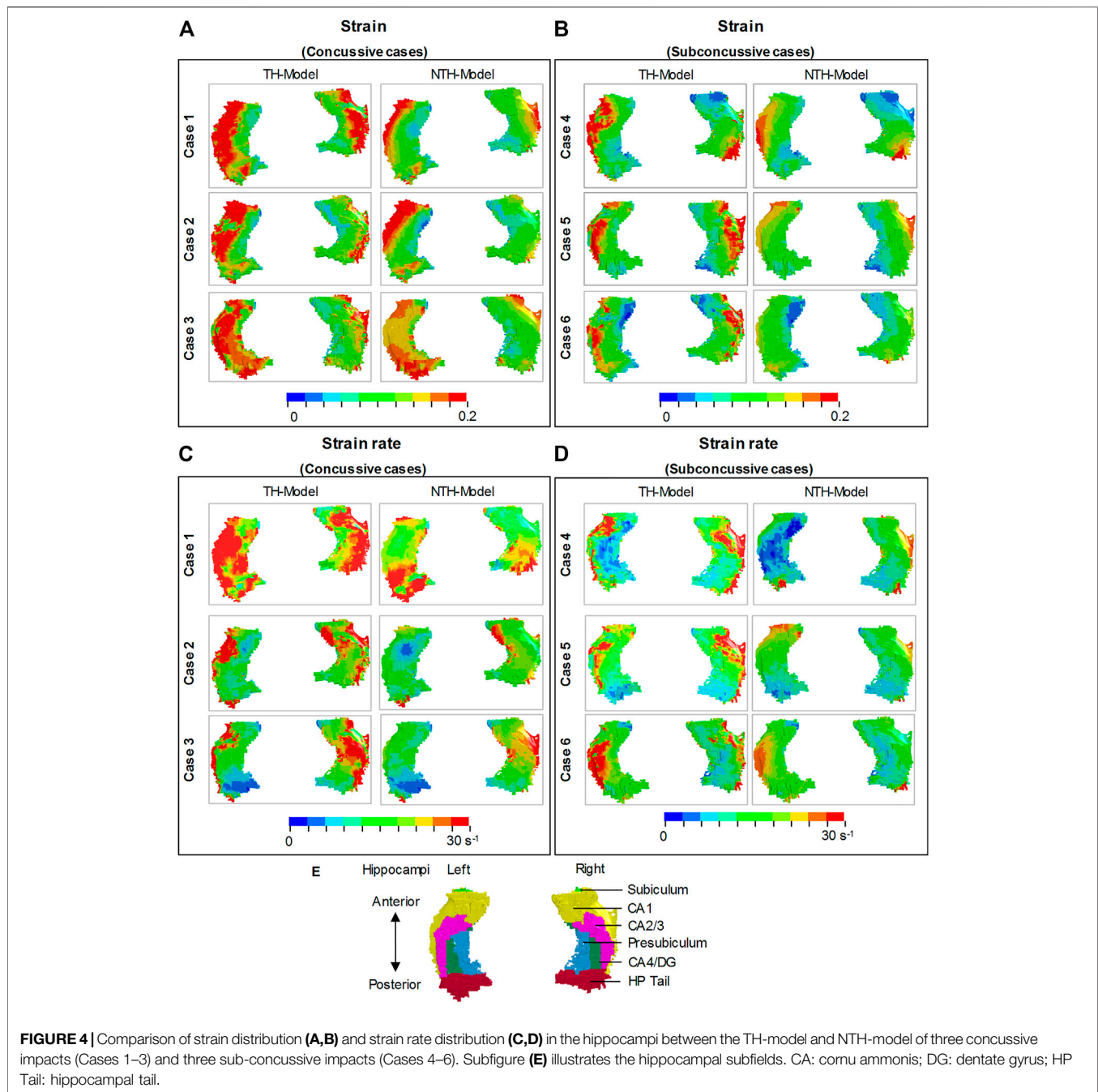sample size, multiple comparisons correction was not performed in the current study.

RESULTS

Strain and Strain Rate in the Hippocampus and Adjacent Structures

We first aimed at elucidating the changes in strain and strain rate distribution due to the presence of the temporal horn. Cross-sections of whole-brain strain and strain rate maps are presented

in **Figure 3**. Almost identical strain and strain rate patterns were predicted by these two models, with the exception of strains over/approaching 0.2 (**Figures 3A,B**) and strain rates over/approaching 30 s^{-1} (**Figures 3C,D**) around the temporal horn that was exclusively predicted by the TH-Model in all simulated loading cases.

Close-up views of hippocampal strain and strain rate contours are presented in **Figure 4**, in which the hippocampal results are shown in **Figure 4A,B** and the anatomical classification of hippocampal subfields is shown in **Figure 4E**. This is particularly evident in CA1, CA2/3, and CA4/DG. Similarly, a
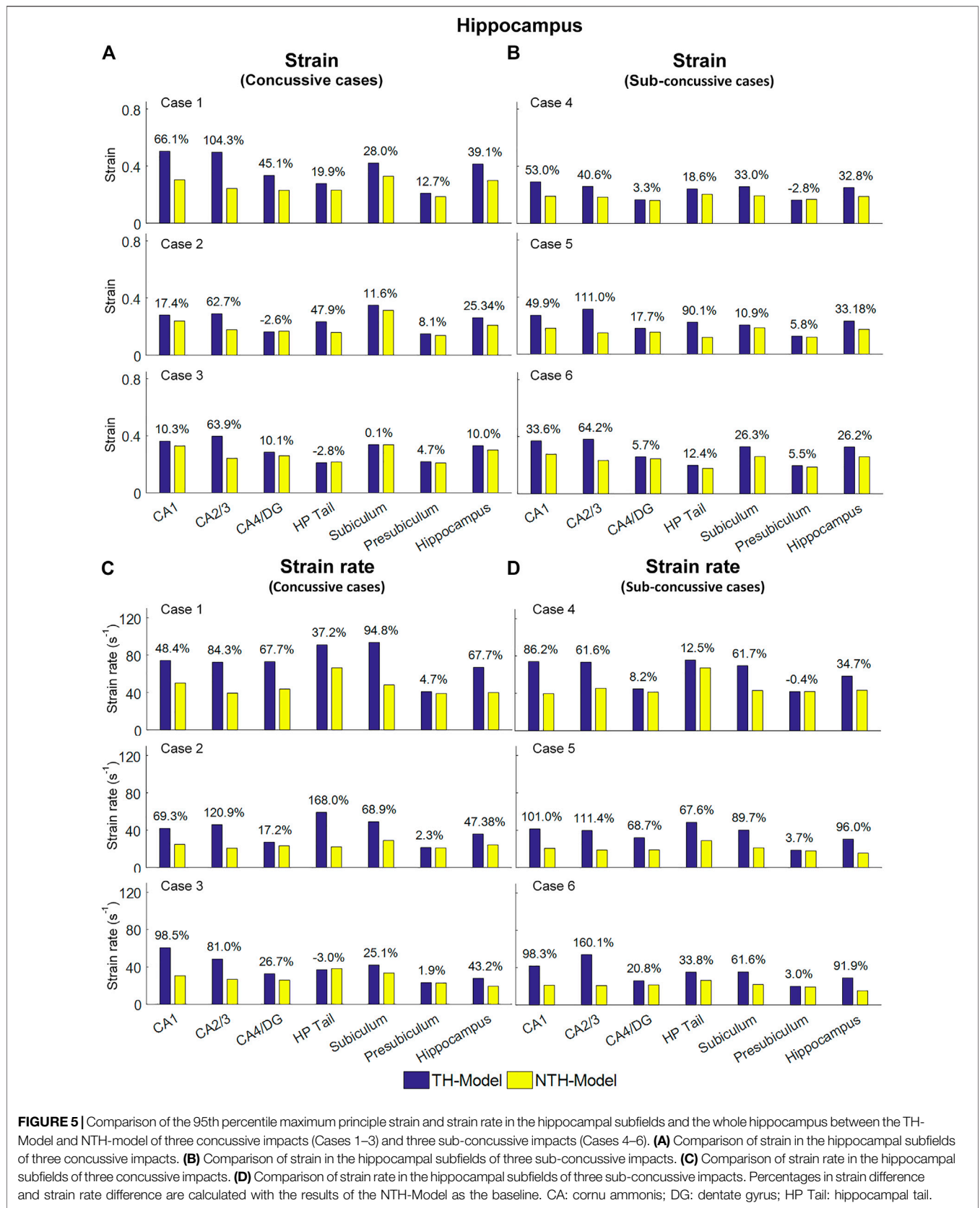
FIGURE 4 | Comparison of strain distribution **(A,B)** and strain rate distribution **(C,D)** in the hippocampi between the TH-model and NTH-model of three concussive impacts (Cases 1–3) and three sub-concussive impacts (Cases 4–6). Subfigure **(E)** illustrates the hippocampal subfields. CA: cornu ammonis; DG: dentate gyrus; HP Tail: hippocampal tail.

more widespread distribution of strain rate approaching or over $30 \, s^{-1}$ was predicted by the TH-Model than the NTH-Model (**Figures 4C,D**) in CA1, CA2/3, and HP Tail. This visual observation is quantitatively confirmed in **Supplementary Appendix SAD**, in which larger volume ratios of strain over 0.2 and strain rate over $30 \, s^{-1}$ in the hippocampal subfields and the whole hippocampal level were predicted by the TH-Model with respect to the NTH-Model.

Figure 5 shows a quantitative depiction of the findings in **Figure 4** with special focus on the peaking values: the addition of the temporal horn elevated the 95th percentile maximum

principal strain for almost all subfields and the whole hippocampus under all loading cases with the largest elevation (111.0%) noted in CA2/3 in Case 5 (**Figures 5A,B**). Similarly, the 95th percentile maximum strain rate was increased per the addition of the temporal horn for almost all hippocampal subfields and the whole hippocampus, with the largest increase (168.0%) in HP Tail in Case 2 (**Figures 5C,D**). Any decrements in strain or strain rate were less than 5%.

We next aimed at identifying the anatomical regions most affected by the presence of the temporal horn. Using a Wilcoxon matched-pairs signed-rank tests on the region-wise strain and

FIGURE 5 | Comparison of the 95th percentile maximum principle strain and strain rate in the hippocampal subfields and the whole hippocampus between the TH-Model and NTH-model of three concussive impacts (Cases 1–3) and three sub-concussive impacts (Cases 4–6). **(A)** Comparison of strain in the hippocampal subfields of three concussive impacts. **(B)** Comparison of strain in the hippocampal subfields of three sub-concussive impacts. **(C)** Comparison of strain rate in the hippocampal subfields of three concussive impacts. **(D)** Comparison of strain rate in the hippocampal subfields of three sub-concussive impacts. Percentages in strain difference and strain rate difference are calculated with the results of the NTH-Model as the baseline. CA: cornu ammonis; DG: dentate gyrus; HP Tail: hippocampal tail.

TABLE 3 | Wilcoxon matched-pairs signed-rank test on the region-wise strain and strain rate in the hippocampal subfields and whole hippocampus **(A)** and non-hippocampal regions **(B)** (N = 6). Percentages in strain difference and strain rate difference between the TH-Model and NTH-model were calculated across all simulations and presented in the form of median and two quartile values with Q1 as 25th percentile value and Q3 as 75th percentile value. Note that N equals to the number of impacts simulated by each model. CA: cornu ammonis; DG: dentate gyrus; HP Tail: hippocampal tail; Ventral DC: ventral diencephalon; CC: corpus callosum.

A	Regions	Percentage in strain difference [median (Q1, Q3)] (%)		p	Percentage in strain rate difference [median (Q1, Q3)] (%)		p
	CA1	44.6	(33.6, 53.0)	0.028	92.3	(69.3, 98.5)	0.028
	CA2/3	64.6	(62.7, 104.3)	0.028	97.9	(81.0, 121.0)	0.028
	CA4/DG	11.7	(3.2, 21.8)	0.046	23.7	(17.2, 67.6)	0.028
	HP Tail	33.9	(18.6, 54.3)	0.046	35.5	(12.5, 67.6)	0.046
	Subiculum	6.9	(5.5, 11.2)	0.046	65.3	(61.6, 89.7)	0.028
	Presubiculum	19.9	(11.6, 28.0)	0.028	2.7	(1.9, 3.7)	0.046
	Hippocampus	29.5	(25.3, 33.2)	0.028	57.5	(34.7, 91.9)	0.028
B	Regions	Percentage in strain difference [median (Q1, Q3)] (%)		p	Percentage in strain rate difference [median (Q1, Q3)] (%)		p
	Amygdala	33.8	(17.1, 39.3)	0.028	50.9	(40.4, 56.1)	0.028
	Ventral DC	8.2	(4.6, 12.2)	0.028	9.35	(3.7, 13.1)	0.028
	Pallidum	−1.7	(−4.2, 2.1)	0.249	−0.6	(−4.2, 4.4)	0.753
	Putamen	−1.4	(−2.3, 2.8)	0.249	2.2	(−0.4, 4.7)	0.173
	Caudate	1.5	(0.7, 5.5)	0.917	0.1	(−2.5, 0.9)	0.463
	CC	0.7	(0.0, 1.3)	0.249	2.5	(−0.4, 3.6)	0.116

strain rate, we found considerable increases in strain (median value of percent strain difference >5%) on all six hippocampal subfields and the whole hippocampus at significant levels ($p < 0.05$) (**Table 3A**). For the strain rate, considerable increases (median value of percent strain rate difference >5%) were noted in all subfields except for the presubiculum.

Among the non-hippocampal regions, both strain and strain rate were elevated in the TH-Model in the amygdala, which is along the anterosuperior border of the temporal horn, and to a lesser extent in the nearby ventral DC (**Supplementary Appendix SAE**, **Table 3B**). For the remaining more-distant regions, percentage differences in strain and strain rate were constantly less than 5% across the simulated loading cases.
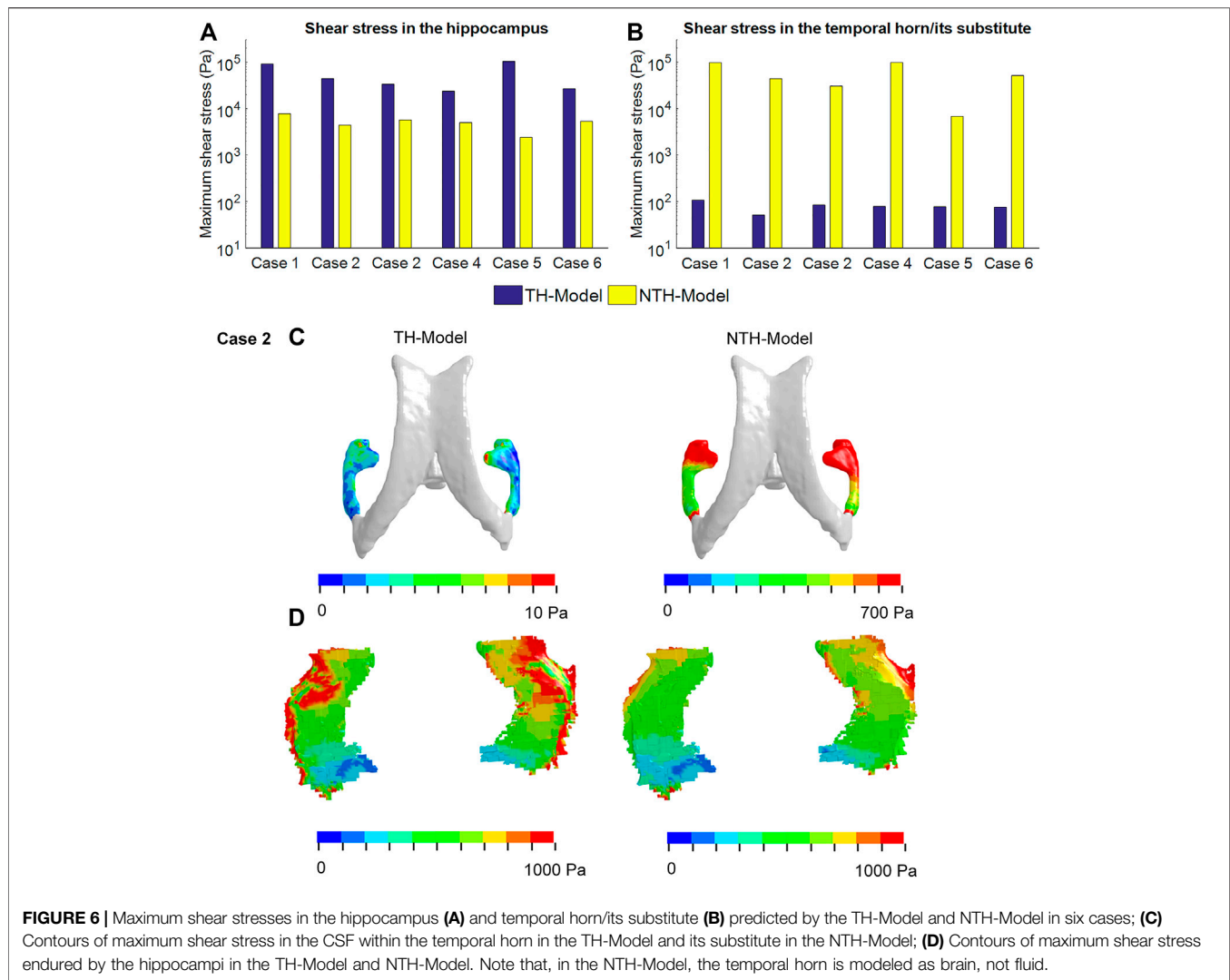
Stress in Hippocampus and Temporal Horn

We then went on to explain the biomechanical reason for the hippocampal vulnerability. To ascertain the alteration of stress transmission associated **Figures 6A,B** with the temporal horn, **Figures 6A,B** illustrates the maximum shear stress (i.e., a force triggering critical tissue deformation) endured by the temporal horn and hippocampus in the TH-Model and their counterparts in the NTH-Model, respectively. A much larger magnitude of shear stress in the hippocampus was noted in the TH-Model compared to the NTH-Model across all the cases (**Figure 6A**). Conversely, the maximum shear stresses were less than 100 Pa in the temporal horn in the TH-Model, and over 1,000 Pa in the temporal horn substitute in the NTH-Model (**Figure 6B**). In addition, the distribution of shear stress within the hippocampus and temporal horn for one representative case (Case 2) are illustrated in **Figures 6C,D**, in which a wider distribution of shear stress over 1,000 Pa in the hippocampus was noted in the TH-Model compared to the NTH-Model. It is thus indicated that an altered stress transmission associated with the temporal horn causes elevations in strain and strain rate.

DISCUSSION

The current study attempted to elucidate why the hippocampus is so commonly affected by brain trauma. We used two FE models: one with and the other without the temporal horn, and incorporated an anatomically accurate description of temporal horn, a mechanically realistic representation of intraventricular CSF as fluid elements, and a fluid-structure interaction coupling approach for the brain-ventricle interface. The presence of the temporal horn not only extended the distribution of high strains and strain rates in the surrounding area, but also increased their magnitude in the hippocampus, particularly in the subfields of CA1, CA2/3, HP Tail, subiculum, and presubiculum. Other adjacent regions including the amygdala and ventral DC showed similarly increased strain and strain rate with the presence of the temporal horn, but distant regions (e.g., corpus callosum) did not. These computational findings suggest that the presence of the temporal horn likely exacerbates the biomechanical vulnerability of the hippocampus following head impacts.

This biomechanical finding correlates well with the prevalence of hippocampal trauma in humans data and animal biomechanical models. Several postmortem neuropathological studies (Kotapka et al., 1992; Kotapka et al., 1993; Kotapka et al., 1994; Maxwell et al., 2003) have detected overt neuronal damage/loss in the hippocampus of TBI victims with high incidence rates up to 73%–87% (although the exact loadings endured were lacking). Animal models employing custom-built pneumatic devices that deliver impulsive angular accelerations, similar to the loading mode in the current study, have shown hippocampal lesions in non-human primates (Gennarelli et al., 1982; Kotapka et al., 1991), which have a similar hippocampal morphology and spatial relationship to the temporal horn (Insausti and Amaral, 2003; Amaral et al., 2007). A version of

FIGURE 6 | Maximum shear stresses in the hippocampus **(A)** and temporal horn/its substitute **(B)** predicted by the TH-Model and NTH-Model in six cases; **(C)** Contours of maximum shear stress in the CSF within the temporal horn in the TH-Model and its substitute in the NTH-Model; **(D)** Contours of maximum shear stress endured by the hippocampi in the TH-Model and NTH-Model. Note that, in the NTH-Model, the temporal horn is modeled as brain, not fluid.

the device modified to deliver impulsive loading caused selective hippocampal damage to porcine brains (Smith et al., 1997) [which again have a similar relationship between the hippocampus and temporal horn to humans (Félix et al., 1999)]. Thus, animal models with similar morphological relationships between the temporal horn and hippocampus support a biomechanical link between the two.

Our computational results predicted an altered stress transmission associated with the temporal horn, providing an explanation for the elevations in strain and strain rate in the TH-Model. As illustrated in **Figure 6B**, the shear stress endured by temporal horn in the TH-Model was less than 100 Pa, which realistically reflected the low shear resistance nature of CSF. Comparatively, the shear stress experienced by the substitute of the temporal horn (i.e., brain parenchyma) in the NTH-Model was over 1,000 Pa, providing an unrealistic interaction with the neighboring tissue. These regions adjacent to the temporal horn (such as the hippocampus, amygdala, and ventral DC, as are the ROIs in the current study) were easier to deform when associated with the addition of the temporal horn in the TH-Model,

consequently exacerbating the strain and strain rate in these ROIs. This explanation was further verified in **Figure 6A**, where the shear stress endured by the hippocampus was larger in the TH-Model, consistent with an amplified force exerted on the hippocampus with the addition of the temporal horn.

Two previous computational studies simulated football head impacts, consistently reporting an increased susceptibility of the hippocampus to injury (Viano et al., 2005; Zhao et al., 2017). However, the ventricular elements in these two models and other ones (Kleiven, 2007; Mao et al., 2013; Atsumi et al., 2018; Trotta et al., 2020) were manually picked with reference to the brain atlas, lacking mesh conformity of the anatomic ventricle profile. Our work used a novel FE model of the brain that involves orders of magnitude more elements than used in typical models (e.g., millions instead of thousands), enabling a realistic depiction of the geometrical features of the temporal horn. Intraventricular CSF elements in existing head models (Viano et al., 2005; Kimpara et al., 2006; Takhounts et al., 2008; Mao et al., 2013; Ho et al., 2017; Zhao et al., 2017; Zhou et al., 2019a; Li et al., 2020) are predominantly represented by Lagrangian elements, with the

mesh following the material deformation without material advection, neglecting the potential fluid flow during the impact. Here, we leveraged a fluid element formulation (i.e., ALE multi-material formulation) for the cerebral ventricle, emulating the fluid properties of intraventricular CSF and potential fluid flow following external stimuli. To couple the mechanical responses of the ALE-represented ventricular CSF elements with the Lagrangian-represented brain elements, a penalty-based coupling was implemented. Such a coupling algorithm permits relative motion in the tangential direction and delivers tension and compression in the radial direction, circumventing severe element distortion at the interfacial boundary. The FSI approach excels in not only realistically representing the fluid behavior of the CSF but also maintaining numerical stability without causing severe element distortion, supporting its validity for the current application. Nevertheless, it is worth clarifying that our data suggest that omitting the temporal horn, as is the case in most existing head models, may still be acceptable for these studies that focus on regions far from the temporal horn (e.g., corpus callosum, caudate, putamen, pallidum).

Hippocampal cell death tolerance criteria were presented by Cater et al. (2006) by relating three independent variables (i.e., strain in the range of 0.05–0.5, hippocampal subfields, time post-injury) to resultant cell death under *in vitro* conditions via mathematical equations, which were valid within the strain rate regime of 0.1–50 s^{-1}. Similarly, another *in vitro* study reported tolerance criteria for hippocampal function impairment in the form of mathematical formulations between input mechanical stimuli (i.e., strain up to 0.44 and strain rate up to 30 s^{-1}) and output electrophysiological alterations (Kang and Morrison, 2015). In the current study, the hippocampal responses predicted by the TH-Model peaking from 0.29 to 0.50 for strain and from 53.9 s^{-1} to 93.6 s^{-1} for strain rate in the six simulated impacts. The range of FE-derived strains and strain rates reached the criteria of electrophysiological impairment and cell death as aforementioned. However, it should be noted that certain disparities existed between the data ranges of the current computational results and the loading regimes from which these two hippocampus-related tolerance criteria were fitted. Moreover, the cultured hippocampal slices in Cater et al. (2006) and Kang and Morrison (2015) were obtained from the rat brain. Extrapolation of the tolerance criteria derived from the animal brain under *in vitro* conditions to the human brain under *in vivo* conditions requires further verification (Seok et al., 2013).

While the presence of the CSF-filled temporal horn may be a contributing factor for the hippocampal vulnerability, additional mechanisms, such as the selective vulnerability of hippocampal neurons to hypoxemia and ischemia (Pulsinelli, 1985; Ng et al., 1989) and pathological neuronal excitation involving glutamate and other excitatory amino acid neurotransmitters (Faden et al., 1989; Bullock et al., 1990), may play important roles in human hippocampal injury. We suggest that the adverse effects of the temporal horn during the primary impact, the superimposed hypoxia/ischemia and neuroexcitotoxicity secondary to the impact, as well as other potential unknown mechanisms, collectively contribute to the hippocampal vulnerability.

Limitations and Future Work

Although the current study yielded some new insights into the biomechanical dependency of the hippocampus on the temporal horn, certain limitations exist which require further investigation. First, only six representative sports-related inertial impacts were simulated in the current study with the severities at concussive and sub-concussive levels. A systematic investigation that covers more impact-related variables (e.g., impact duration, impact directions, rotational velocity) with their magnitudes spanning over the regimes measured from the realistic impacts is planned for future work to identify the critical scenarios that the temporal horn exhibited a more pronounced effect on the hippocampus. Moreover, caution should be exercised when extrapolating the current findings obtained from concussive and sub-concussive impacts to extra injury scenarios (e.g., fatal brain injury, penetrating head injury).

Another aspect of limitation was that multiple comparison correction were not conducted. In the statistical analysis, 26 comparisons were respectively performed based on the strain and strain rate results from 13 ROIs, each of which results from six impact simulations predicted by the TH-Model and NTH-Model were paired and analyzed using a significance threshold of 0.05. Given that we did not perform multiple comparison correction, there might be a chance up to 74% that at least one of the comparisons indicating a statistically significance may not be the case in fact.

Thirdly, due to the computational challenges, the brain-skull interfaces in both models in the current study were simulated by approximating the subarachnoid CSF as a Lagrangian-represented structure. Given that the ROIs in the current study are all located at central brain regions, the influence exerted by the brain-skull influence on the deep brain structures was expected to be limited (Kleiven and Hardy, 2002). Per the benefits of using ALE elements for the cerebral ventricles, the impact-induced fluid flow was considered, but not quantified in the current study. A detailed examination of flow patterns of CSF remains to be appropriately quantified in the future (Lang and Wu, 2021).

Fourthly, to incorporate explicit representations of the hippocampal subfields in the FE models, Freesurfer was used to segment the MRI with a resolution of $1 \times 1 \times 1$ mm^3 to take advantage of the isotropic high-resolution atlas and incorporate this detailed isotropic segmentation into the FE model. Such a software choice was for the consistency purpose, since the brain profile used for the development of FE model was obtained from Freesurfer. However, it should be highlighted there are many different segmentation methods for hippocampal subfields, presenting certain variances in specific subfield delineation (Yushkevich et al., 2015; Wisse et al., 2021). Thus, caution should be exercised when using Freesurfer for hippocampal subfield segmentation (Wisse et al., 2014). In fact, there appear no approaches with guaranteed utility and validity to segment hippocampal subfield from isotropic 1 mm^3 MRI (Wisse et al., 2021), as is the case for the subfield delineation in the FE model. This segment-induced error inevitably compromised the accuracy of hippocampal subfield representations in the FE model, which is a limitation of the current study. Nevertheless, compared with the studies in which

the hippocampus was treated as a single medium (Takhounts et al., 2008; Mao et al., 2013; Miller et al., 2016; Atsumi et al., 2018; Zhou et al., 2020a; Li et al., 2020; Trotta et al., 2020), the current work made the first step to differentiate the hippocampal substructures in the FE model of the human brain. Future work is planned to further refine the model towards an anatomically more authentic hippocampal subfield representation.

Lastly, due to the lack of neuroimaging data of these players with their head impacts being simulated, it is hardly possible to ascertain whether hippocampal injury indeed occurred in these six simulated impacts. At Stanford, ongoing effort is dedicated to deploy instrumented mouthguards to football players, obtaining real-time measurements of the impacts sustained by these players (Camarillo et al., 2013; Hernandez et al., 2015; Domel et al., 2021; Liu et al., 2020). This information is complemented by medical imaging of the football players pre- and post-impact (Parivash et al., 2019; Mills et al., 2020). Findings in the current work will be further testified by correlating on-field football impacts, to computationally predicted hippocampal deformation, to image-based evidence of hippocampal injury.

CONCLUSION

This study investigated the biomechanical mechanism of hippocampal injury associated with the presence of the temporal horn by leveraging two models, with and without the inclusion of the temporal horn. The results showed that the temporal horn has a significant biomechanical effect in the surrounding area and induces increased magnitudes of the strain and strain rate in the hippocampus throughout its subfields, identifying the temporal horn as a contributing factor to the hippocampal vulnerability. This study suggests that proper modeling of the temporal horn be considered when developing mechanical tolerance and designing protective strategies specifically for the hippocampus.

DATA AVAILABILITY STATEMENT

The original contributions presented in the study are included in the article/**Supplementary Material**, further inquiries can be directed to the corresponding authors.

AUTHOR CONTRIBUTIONS

Conception and design of the study: ZZ, XL, AD, ED, SK, MG, DC, and MZ; Computational simulation and data analysis: ZZ, XL, AD, YL, SR, SK, DC, and MZ; Acquisition and analysis of the imaging data: ED, MG, GG, DC, and MZ; Drafting significant portion of the manuscript and figures: ZZ, XL, MG, and MZ.

FUNDING

ACKNOWLEDGMENTS

SUPPLEMENTARY MATERIAL

The Supplementary Material for this article can be found online at: https://www.frontiersin.org/articles/10.3389/fbioe.2022.754344/full#supplementary-material

REFERENCES

Aimedieu, P., and Grebe, R. (2004). Tensile Strength of Cranial Pia Mater: Preliminary Results. *J. Neurosurg.* 100, 111–114. doi:10.3171/jns.2004.100.1.0111

Amaral, D., Andersen, P., O'keefe, J., and Morris, R. (2007). *The hippocampus Book*. Oxford, United Kingdom: Oxford University Press.

Anderson, R. W. G., Brown, C. J., Blumbergs, P. C., Mclean, A. J., and Jones, N. R. (2003). Impact Mechanics and Axonal Injury in a Sheep Model. *J. Neurotrauma* 20, 961–974. doi:10.1089/089771503770195812

Atsumi, N., Nakahira, Y., Tanaka, E., and Iwamoto, M. (2018). Human Brain Modeling with its Anatomical Structure and Realistic Material Properties for Brain Injury Prediction. *Ann. Biomed. Eng.* 46, 736–748. doi:10.1007/s10439-018-1988-8

Baldwin, S. A., Gibson, T., Callihan, C. T., Sullivan, P. G., Palmer, E., and Scheff, S. W. (1997). Neuronal Cell Loss in the CA3 Subfield of the hippocampus Following Cortical Contusion Utilizing the Optical Disector Method for Cell Counting. *J. Neurotrauma* 14, 385–398. doi:10.1089/neu.1997.14.385

Batterbee, D. C., Sims, N. D., Becker, W., Worden, K., and Rowson, J. (2011). Computational Model of an Infant Brain Subjected to Periodic Motion Simplified Modelling and Bayesian Sensitivity Analysis. *Proc. Inst. Mech. Eng. H* 225, 1036–1049. doi:10.1177/0954411911420002

Bigler, E. D., Anderson, C. V., Blatter, D. D., and Andersob, C. V. (2002). Temporal Lobe Morphology in normal Aging and Traumatic Brain Injury. *AJNR Am. J. Neuroradiol.* 23, 255–266.

Bigler, E. D., Blatter, D. D., Anderson, C. V., Johnson, S. C., Gale, S. D., Hopkins, R. O., et al. (1997). Hippocampal Volume in normal Aging and Traumatic Brain Injury. *AJNR Am. J. Neuroradiol.* 18, 11–23.

Bigler, E. D., and Tate, D. F. (2001). Brain Volume, Intracranial Volume, and Dementia. *Invest. Radiol.* 36, 539–546. doi:10.1097/00004424-200109000-00006

Bird, C. M., and Burgess, N. (2008). The hippocampus and Memory: Insights from Spatial Processing. *Nat. Rev. Neurosci.* 9, 182–194. doi:10.1038/nrn2335

Bullock, R., Butcher, S., and Mcculloch, J. (1990). "Changes in Extracellular Glutamate Concentration after Acute Subdural Haematoma in the Rat - Evidence for an "Excitotoxic" Mechanism," in *Brain Edema VIII*. Editors H.-J. Reulen, A. Baethmann, J. Fenstermacher, A. Marmarou, and M. Spatz (Berlin/Heidelberg, Germany: Springer), 274–276. doi:10.1007/978-3-7091-9115-6_93

Camarillo, D. B., Shull, P. B., Mattson, J., Shultz, R., and Garza, D. (2013). An Instrumented Mouthguard for Measuring Linear and Angular Head Impact Kinematics in American Football. *Ann. Biomed. Eng.* 41, 1939–1949. doi:10.1007/s10439-013-0801-y

Cameron, K. L., Marshall, S. W., Sturdivant, R. X., and Lincoln, A. E. (2012). Trends in the Incidence of Physician-Diagnosed mild Traumatic Brain Injury Among Active Duty U.S. Military Personnel between 1997 and 2007. *J. Neurotrauma* 29, 1313–1321. doi:10.1089/neu.2011.2168

Cater, H. L., Sundstrom, L. E., and Morrison, B., Iii (2006). Temporal Development of Hippocampal Cell Death Is Dependent on Tissue Strain but Not Strain Rate. *J. Biomech.* 39, 2810–2818. doi:10.1016/j.jbiomech.2005.09.023

Cecchi, N. J., Domel, A. G., Liu, Y., Rice, E., Lu, R., Zhan, X., et al. (2021). Identifying Factors Associated with Head Impact Kinematics and Brain Strain in High School American Football via Instrumented Mouthguards. *Ann. Biomed. Eng.* 49 (10), 2814–2826. doi:10.1007/s10439-021-02853-5

Dewan, M. C., Rattani, A., Gupta, S., Baticulon, R. E., Hung, Y. C., Punchak, M., et al. (2018). Estimating the Global Incidence of Traumatic Brain Injury. *J. Neurosurg.* 130, 1–18. doi:10.3171/2017.10.JNS17352

Domel, A. G., Raymond, S. J., Giordano, C., Liu, Y., Yousefsani, S. A., Fanton, M., et al. (2021). A New Open-Access Platform for Measuring and Sharing mTBI Data. *Scientific Reports* 11, 7501. doi:10.1038/s41598-021-87085-2

Faden, A. I., Demediuk, P., Panter, S. S., and Vink, R. (1989). The Role of Excitatory Amino Acids and NMDA Receptors in Traumatic Brain Injury. *Science* 244, 798–800. doi:10.1126/science.2567050

Félix, B., Léger, M.-E., Albe-Fessard, D., Marcilloux, J.-C., Rampin, O., Laplace, J.-P., et al. (1999). Stereotaxic Atlas of the Pig Brain. *Brain Res. Bull.* 49, 1–137. doi:10.1016/s0361-9230(99)00012-x

Fillmore, P. T., Phillips-Meek, M. C., and Richards, J. E. (2015). Age-specific MRI Brain and Head Templates for Healthy Adults from 20 through 89 Years of Age. *Front. Aging Neurosci.* 7, 44. doi:10.3389/fnagi.2015.00044

Fischl, B. (2012). FreeSurfer. *NeuroImage* 62, 774–781. doi:10.1016/j.neuroimage.2012.01.021

Gabler, L. F., Crandall, J. R., and Panzer, M. B. (2018). Development of a Metric for Predicting Brain Strain Responses Using Head Kinematics. *Ann. Biomed. Eng.* 46, 972–985. doi:10.1007/s10439-018-2015-9

Gale, S. D., Johnson, S. C., Bigler, E. D., and Blatter, D. D. (1994). Traumatic Brain Injury and Temporal Horn Enlargement: Correlates with Tests of Intelligence and Memory. *Neuropsychiatry, Neuropsychol. Behav. Neurol.* 7, 160–165.

Gennarelli, T. A., Thibault, L. E., Adams, J. H., Graham, D. I., Thompson, C. J., and Marcincin, R. P. (1982). Diffuse Axonal Injury and Traumatic Coma in the Primate. *Ann. Neurol.* 12, 564–574. doi:10.1002/ana.410120611

Graham, D. I., Adams, J. H., and Doyle, D. (1978). Ischaemic Brain Damage in Fatal Non-missile Head Injuries. *J. Neurol. Sci.* 39, 213–234. doi:10.1016/0022-510x(78)90124-7

Graham, D. I., Ford, I., Adams, J. H., Doyle, D., Teasdale, G. M., Lawrence, A. E., et al. (1989). Ischaemic Brain Damage Is Still Common in Fatal Non-missile Head Injury. *J. Neurol. Neurosurg. Psychiatry* 52, 346–350. doi:10.1136/jnnp.52.3.346

Hajiaghamemar, M., Wu, T., Panzer, M. B., and Margulies, S. S. (2020). Embedded Axonal Fiber Tracts Improve Finite Element Model Predictions of Traumatic Brain Injury. *Biomech. Model. Mechanobiol* 19, 1109–1130. doi:10.1007/s10237-019-01273-8

Hallquist, J. O. (2007). *LS-DYNA Keyword User's Manual*. Livermore, California, United States: Livermore Software Technology Corporation.

Hardy, W. N., Mason, M. J., Foster, C. D., Shah, C. S., Kopacz, J. M., Yang, K. H., et al. (2007). A Study of the Response of the Human Cadaver Head to Impact. *Stapp Car Crash J.* 51, 17–80. doi:10.4271/2007-22-0002

Hernandez, F., Wu, L. C., Yip, M. C., Laksari, K., Hoffman, A. R., Lopez, J. R., et al. (2015). Six Degree-Of-freedom Measurements of Human Mild Traumatic Brain Injury. *Ann. Biomed. Eng.* 43, 1918–1934. doi:10.1007/s10439-014-1212-4

Hicks, R., Soares, H., Smith, D., and Mcintosh, T. (1996). Temporal and Spatial Characterization of Neuronal Injury Following Lateral Fluid-Percussion Brain Injury in the Rat. *Acta Neuropathologica* 91, 236–246. doi:10.1007/s004010050421

Ho, J., Zhou, Z., Li, X., and Kleiven, S. (2017). The peculiar Properties of the Falx and Tentorium in Brain Injury Biomechanics. *J. Biomech.* 60, 243–247. doi:10.1016/j.jbiomech.2017.06.023

Holzapfel, A. G. (2000). *Nonlinear Solid Mechanics II*. New Jersey, United States: Wiley. Hoboken.

Insausti, R., and Amaral, D. G. (2003). "Hippocampal Formation," in *The Human Nervous System*. Editors J. K. Mai, J. Assheuer, and G. Paxinos. Second Edition (Amsterdam, Netherlands: Elsevier), 871–914.

Ji, S., Zhao, W., Ford, J. C., Beckwith, J. G., Bolander, R. P., Greenwald, R. M., et al. (2015). Group-wise Evaluation and Comparison of white Matter Fiber Strain and Maximum Principal Strain in Sports-Related Concussion. *J. Neurotrauma* 32, 441–454. doi:10.1089/neu.2013.3268

Kalish, B. T., and Whalen, M. J. (2016). "Weight Drop Models in Traumatic Brain Injury," in *Injury Models of the central Nervous System*. Editors F. H. Kobeissy, C. E. Dixon, R. L. Hayes, and S. Mondello (Berlin/Heidelberg, Germany: Springer), 193–209. doi:10.1007/978-1-4939-3816-2_12

Kang, W. H., and Morrison, B. (2015). Functional Tolerance to Mechanical Deformation Developed from Organotypic Hippocampal Slice Cultures. *Biomech. Model. Mechanobiol.* 14, 561–575. doi:10.1007/s10237-014-0622-4

Kimpara, H., Nakahira, Y., Iwamoto, M., Miki, K., Ichihara, K., Kawano, S., et al. (2006). Investigation of Anteroposterior Head-Neck Responses during Severe Frontal Impacts Using a Brain-Spinal Cord Complex FE Model. *Stapp Car Crash J.* 50, 509–544. doi:10.4271/2006-22-0019

Kleiven, S., and Hardy, W. N. (2002). Correlation of an FE Model of the Human Head with Local Brain Motion--Consequences for Injury Prediction. *Stapp Car Crash J.* 46, 123–144. doi:10.4271/2002-22-0007

Kleiven, S. (2007). Predictors for Traumatic Brain Injuries Evaluated through Accident Reconstructions. *Stapp Car Crash J.* 51, 81–114. doi:10.4271/2007-22-0003

Kotapka, M. J., Gennarelli, T. A., Graham, D. I., Adams, J. H., Thibault, L. E., Ross, D. T., et al. (1991). Selective Vulnerability of Hippocampal Neurons in Acceleration-Induced Experimental Head Injury. *J. Neurotrauma* 8, 247–258. doi:10.1089/neu.1991.8.247

Kotapka, M. J., Graham, D. I., Adams, J. H., Doyle, D., and Gennarelli, T. A. (1993). Hippocampal Damage in Fatal Paediatric Head Injury. *Neuropathol. Appl. Neurobiol.* 19, 128–133. doi:10.1111/j.1365-2990.1993.tb00417.x

Kotapka, M. J., Graham, D. I., Adams, J. H., and Gennarelli, T. A. (1994). Hippocampal Pathology in Fatal Human Head Injury without High Intracranial Pressure. *J. Neurotrauma* 11, 317–324. doi:10.1089/neu.1994.11.317

Kotapka, M. J., Graham, D. I., Adams, J. H., and Gennarelli, T. A. (1992). Hippocampal Pathology in Fatal Non-missile Human Head Injury. *Acta Neuropathol.* 83, 530–534. doi:10.1007/bf00310031

Lang, J., and Wu, Q. (2021). Modelling of the Transient Cerebrospinal Fluid Flow under External Impacts. *Eur. J. Mechanics-B/Fluids* 87. doi:10.1016/j.euromechflu.2021.01.010

Langlois, J. A., and Sattin, R. W. (2005). Preface. *J. Head Trauma Rehabil.* 20, 187–188. doi:10.1097/00001199-200505000-00001

Leranth, C., Szeidemann, Z., Hsu, M., and Buzsáki, G. (1996). AMPA Receptors in the Rat and Primate hippocampus: a Possible Absence of GluR2/3 Subunits in Most Interneurons. *Neuroscience* 70, 631–652. doi:10.1016/s0306-4522(96)83003-x

Li, X., Zhou, Z., and Kleiven, S. (2020). An Anatomically Detailed and Personalizable Head Injury Model: Significance of Brain and white Matter Tract Morphological Variability on Strain. *Biomech. Model. Mechanobiology* 20, 403–431. doi:10.1007/s10237-020-01391-8

Liu, Y., Domel, A. G., Yousefsani, S. A., Kondic, J., Grant, G., Zeineh, M., et al. (2020). Validation and Comparison of Instrumented Mouthguards for Measuring Head Kinematics and Assessing Brain Deformation in Football Impacts. *Ann. Biomed. Eng.* 48, 2580–2598. doi:10.1007/s10439-020-02629-3

Maas, A. I. R., Menon, D. K., Adelson, P. D., Andelic, N., Bell, M. J., Belli, A., et al. (2017). Traumatic Brain Injury: Integrated Approaches to Improve Prevention, Clinical Care, and Research. *Lancet Neurol.* 16, 987–1048. doi:10.1016/S1474-4422(17)30371-X

Mao, H., Zhang, L., Jiang, B., Genthikatti, V. V., Jin, X., Zhu, F., et al. (2013). Development of a Finite Element Human Head Model Partially Validated with

Thirty Five Experimental Cases. *J. Biomech. Eng.* 135, 111002. doi:10.1115/1.4025101

Maréchal, L. (2009). "Advances in Octree-Based All-Hexahedral Mesh Generation: Handling Sharp Features," in *Proceedings of the 18th International Meshing Roundtable*. Editor B. W. Clark (Berlin/Heidelberg, Germany: Springer), 65–84. doi:10.1007/978-3-642-04319-2_5

Maxwell, W. L., Dhillon, K., Harper, L., Espin, J., Macintosh, T. K., Smith, D. H., et al. (2003). There Is Differential Loss of Pyramidal Cells from the Human hippocampus with Survival after blunt Head Injury. *J. Neuropathol. Exp. Neurol.* 62, 272–279. doi:10.1093/jnen/62.3.272

Mcallister, T. W., Ford, J. C., Ji, S., Beckwith, J. G., Flashman, L. A., Paulsen, K., et al. (2012). Maximum Principal Strain and Strain Rate Associated with Concussion Diagnosis Correlates with Changes in Corpus Callosum white Matter Indices. *Ann. Biomed. Eng.* 40, 127–140. doi:10.1007/s10439-011-0402-6

Mckee, A. C., Stein, T. D., Kiernan, P. T., and Alvarez, V. E. (2015). The Neuropathology of Chronic Traumatic Encephalopathy. *Brain Pathol.* 25, 350–364. doi:10.1111/bpa.12248

Meier, T. B., Brummel, B. J., Singh, R., Nerio, C. J., Polanski, D. W., and Bellgowan, P. S. F. (2015). The Underreporting of Self-Reported Symptoms Following Sports-Related Concussion. *J. Sci. Med. Sport* 18, 507–511. doi:10.1016/j.jsams.2014.07.008

Miller, L. E., Urban, J. E., and Stitzel, J. D. (2016). Development and Validation of an Atlas-Based Finite Element Brain Model. *Biomech. Model. Mechanobiol.* 15, 1201–1214. doi:10.1007/s10237-015-0754-1

Mills, B. D., Goubran, M., Parivash, S. N., Dennis, E. L., Rezaii, P., Akers, C., et al. (2020). Longitudinal Alteration of Cortical Thickness and Volume in High-Impact Sports. *NeuroImage* 217, 116864. doi:10.1016/j.neuroimage.2020.116864

Ng, T., Graham, D. I., Adams, J. H., and Ford, I. (1989). Changes in the hippocampus and the Cerebellum Resulting from Hypoxic Insults: Frequency and Distribution. *Acta Neuropathol.* 78, 438–443. doi:10.1007/bf00688181

Panzer, M. B., Myers, B. S., Capehart, B. P., and Bass, C. R. (2012). Development of a Finite Element Model for Blast Brain Injury and the Effects of CSF Cavitation. *Ann. Biomed. Eng.* 40, 1530–1544. doi:10.1007/s10439-012-0519-2

Parivash, S. N., Goubran, M., Mills, B. D., Rezaii, P., Thaler, C., Wolman, D., et al. (2019). Longitudinal Changes in Hippocampal Subfield Volume Associated with Collegiate Football. *J. Neurotrauma* 36, 2762–2773. doi:10.1089/neu.2018.6357

Parsons, C. G., Danysz, W., and Quack, G. (1999). Memantine Is a Clinically Well Tolerated N-Methyl-D-Aspartate (NMDA) Receptor Antagonist-A Review of Preclinical Data. *Neuropharmacology* 38, 735–767. doi:10.1016/s0028-3908(99)00019-2

Pellman, E. J., Viano, D. C., Tucker, A. M., Casson, I. R., and Waeckerle, J. F. (2003). Concussion in Professional Football: Reconstruction of Game Impacts and Injuries. *Neurosurgery* 53, 799–814. doi:10.1093/neurosurgery/53.3.799

Pieper, S., Halle, M., and Kikinis, R. "3D Slicer," in Proceedingd of the 2004 2nd IEEE international symposium on biomedical imaging: nano to macro (IEEE Cat No. 04EX821), Arlington, VA, USA, April 2004 (Piscataway, New Jersey, United States: IEEE), 632–635.

Pulsinelli, W. A. (1985). "Selective Neuronal Vulnerability: Morphological and Molecular Characteristics," in *Progress in Brain Research*. Editor E. Walsh (Amsterdam, Netherlands: Elsevier), 29–37. doi:10.1016/s0079-6123(08)61973-1

Roozenbeek, B., Maas, A. I. R., and Menon, D. K. (2013). Changing Patterns in the Epidemiology of Traumatic Brain Injury. *Nat. Rev. Neurol.* 9, 231–236. doi:10.1038/nrneurol.2013.22

Rosenthal, J. A., Foraker, R. E., Collins, C. L., and Comstock, R. D. (2014). National High School Athlete Concussion Rates from 2005-2006 to 2011-2012. *Am. J. Sports Med.* 42, 1710–1715. doi:10.1177/0363546514530091

Runnerstam, M., Bao, F., Huang, Y., Shi, J., Gutierrez, E., Hamberger, A., et al. (2001). A New Model for Diffuse Brain Injury by Rotational Acceleration: II. Effects on Extracellular Glutamate, Intracranial Pressure, and Neuronal Apoptosis. *J. Neurotrauma* 18, 259–273. doi:10.1089/08977150151070892

Sanchez, E. J., Gabler, L. F., Good, A. B., Funk, J. R., Crandall, J. R., and Panzer, M. B. (2019). A Reanalysis of Football Impact Reconstructions for Head

Kinematics and Finite Element Modeling. *Clin. Biomech.* 64, 82–89. doi:10.1016/j.clinbiomech.2018.02.019

Seok, J., Warren, H. S., Cuenca, A. G., Mindrinos, M. N., Baker, H. V., Xu, W., et al. (2013). Genomic Responses in Mouse Models Poorly Mimic Human Inflammatory Diseases. *Proc. Natl. Acad. Sci. USA* 110, 3507–3512. doi:10.1073/pnas.1222878110

Singh, R., Meier, T. B., Kuplicki, R., Savitz, J., Mukai, I., Cavanagh, L., et al. (2014). Relationship of Collegiate Football Experience and Concussion with Hippocampal Volume and Cognitive Outcomes. *Jama* 311, 1883–1888. doi:10.1001/jama.2014.3313

Smith, D. H., Chen, X.-H., Xu, B.-N., Mcintosh, T. K., Gennarelli, T. A., and Meaney, D. F. (1997). Characterization of Diffuse Axonal Pathology and Selective Hippocampal Damage Following Inertial Brain Trauma in the Pig. *J. Neuropathol. Exp. Neurol.* 56, 822–834. doi:10.1097/00005072-199756070-00009

Souli, M., Ouahsine, A., and Lewin, L. (2000). ALE Formulation for Fluid-Structure Interaction Problems. *Comput. Methods Appl. Mech. Eng.* 190, 659–675. doi:10.1016/s0045-7825(99)00432-6

Takhounts, E. G., Ridella, S. A., Hasija, V., Tannous, R. E., Campbell, J. Q., Malone, D., et al. (2008). Investigation of Traumatic Brain Injuries Using the Next Generation of Simulated Injury Monitor (SIMon) Finite Element Head Model. *Stapp Car Crash J.* 52, 1–31. doi:10.4271/2008-22-0001

Trotta, A., Clark, J. M., Mcgoldrick, A., Gilchrist, M. D., and Annaidh, A. N. (2020). Biofidelic Finite Element Modelling of Brain Trauma: Importance of the Scalp in Simulating Head Impact. *Int. J. Mech. Sci.* 173, 105448. doi:10.1016/j.ijmecsci.2020.105448

Van Leer, B. (1979). Towards the Ultimate Conservative Difference Scheme. V. A Second-Order Sequel to Godunov's Method. *J. Comput. Phys.* 32, 101–136. doi:10.1016/0021-9991(79)90145-1

Van Noort, R., Black, M. M., Martin, T. R. P., and Meanley, S. (1981). A Study of the Uniaxial Mechanical Properties of Human Dura Mater Preserved in Glycerol. *Biomaterials* 2, 41–45. doi:10.1016/0142-9612(81)90086-7

Viano, D. C., Casson, I. R., Pellman, E. J., Zhang, L., King, A. I., and Yang, K. H. (2005). Concussion in Professional Football: Brain Responses by Finite Element Analysis: Part 9. *Neurosurgery* 57, 891–916. doi:10.1227/01.neu.0000186950.54075.3b

Wisse, L. E. M., Biessels, G. J., and Geerlings, M. I. (2014). A Critical Appraisal of the Hippocampal Subfield Segmentation Package in FreeSurfer. *Front. Aging Neurosci.* 6, 261. doi:10.3389/fnagi.2014.00261

Wisse, L. E. M., Chételat, G., Daugherty, A. M., Flores, R., Joie, R., Mueller, S. G., et al. (2021). Hippocampal Subfield Volumetry from Structural Isotropic 1 Mm 3 MRI Scans: A Note of Caution. *Hum. Brain Mapp.* 42, 539–550. doi:10.1002/hbm.25234

Wolf, J. A., Johnson, B. N., Johnson, V. E., Putt, M. E., Browne, K. D., Mietus, C. J., et al. (2017). Concussion Induces Hippocampal Circuitry Disruption in Swine. *J. Neurotrauma* 34, 2303–2314. doi:10.1089/neu.2016.4848

Wu, T., Hajiaghamemar, M., Giudice, J. S., Alshareef, A., Margulies, S. S., and Panzer, M. B. (2021). Evaluation of Tissue-Level Brain Injury Metrics Using Species-specific Simulations. *J. Neurotrauma* 38, 1879–1888. doi:10.1089/neu.2020.7445

Yushkevich, P. A., Amaral, R. S. C., Augustinack, J. C., Bender, A. R., Bernstein, J. D., Boccardi, M., et al. (2015). Quantitative Comparison of 21 Protocols for Labeling Hippocampal Subfields and Parahippocampal Subregions in *In Vivo* MRI: towards a Harmonized Segmentation Protocol. *Neuroimage* 111, 526–541. doi:10.1016/j.neuroimage.2015.01.004

Zhao, W., Cai, Y., Li, Z., and Ji, S. (2017). Injury Prediction and Vulnerability Assessment Using Strain and Susceptibility Measures of the Deep white Matter. *Biomech. Model. Mechanobiol.* 16, 1709–1727. doi:10.1007/s10237-017-0915-5

Zhao, W., and Ji, S. (2019). Mesh Convergence Behavior and the Effect of Element Integration of a Human Head Injury Model. *Ann. Biomed. Eng.* 47, 475–486. doi:10.1007/s10439-018-02159-z

Zhou, Z., Li, X., Kleiven, S., and Hardy, W. N. (2019c). Brain Strain from Motion of Sparse Markers. *Stapp Car Crash J.* 63, 1–27. doi:10.4271/2019-22-0001

Zhou, Z., Domel, A. G., Li, X., Grant, G., Kleiven, S., Camarillo, D., et al. (2021a). White Matter Tract-Oriented Deformation Is Dependent on Real-Time Axonal Fiber Orientation. *J. Neurotrauma* 38, 1730–1745. doi:10.1089/neu.2020.7412

Zhou, Z. (2019). *Evaluation of Fluid-Structure Interaction and Biofidelity of Finite Element Head Models.* Doctor: KTH Royal Institute of Technology.

Zhou, Z., Jiang, B., Cao, L., Zhu, F., Mao, H., and Yang, K. H. (2016). Numerical Simulations of the 10-Year-Old Head Response in Drop Impacts and Compression Tests. *Comput. Methods Programs Biomed.* 131, 13–25. doi:10.1016/j.cmpb.2016.04.013

Zhou, Z., Li, X., and Kleiven, S. (2019a). Biomechanics of Acute Subdural Hematoma in the Elderly: A Fluid-Structure Interaction Study. *J. Neurotrauma* 36, 2099–2108. doi:10.1089/neu.2018.6143

Zhou, Z., Li, X., and Kleiven, S. (2020a). Biomechanics of Periventricular Injury. *J. Neurotrauma* 37, 1074–1090. doi:10.1089/neu.2019.6634

Zhou, Z., Li, X., and Kleiven, S. (2020b). Evaluation of Brain-Skull Interface Modelling Approaches on the Prediction of Acute Subdural Hematoma in the Elderly. *J. Biomech.* 105, 109787. doi:10.1016/j.jbiomech.2020.109787

Zhou, Z., Li, X., and Kleiven, S. (2019b). Fluid-structure Interaction Simulation of the Brain-Skull Interface for Acute Subdural Haematoma Prediction. *Biomech. Model. Mechanobiol.* 18, 155–173. doi:10.1007/s10237-018-1074-z

Zhou, Z., Li, X., Liu, Y., Fahlstedt, M., Georgiadis, M., Zhan, X., et al. (2021b). Toward a Comprehensive Delineation of White Matter Tract-Related Deformation. *J. Neurotrauma* 38, 3260–3278. doi:10.1089/neu.2021.0195